

PAPER • OPEN ACCESS

Insights on the variability of Cu filament formation in the SiO₂ electrolyte of quantized-conductance conductive bridge random access memory devices

To cite this article: Florian Maudet *et al* 2023 *Nanotechnology* **34** 245203

View the [article online](#) for updates and enhancements.

You may also like

- [Conductive bridging random access memory—materials, devices and applications](#)
Michael N Kozicki and Hugh J Barnaby
- [Influence of Interfacial Tantalum Oxynitride on Resistive Switching of Cu/Cu–SiO₂/TaN](#)
Shyankay Jōu and Ming-En Han
- [Effect of oxygen concentration on resistive switching behavior in silicon oxynitride film](#)
Da Chen, Shihua Huang and Lü He

PRIME
PACIFIC RIM MEETING
ON ELECTROCHEMICAL
AND SOLID STATE SCIENCE

HONOLULU, HI
Oct 6–11, 2024

Abstract submission deadline:
April 12, 2024

Learn more and submit!

Joint Meeting of
The Electrochemical Society
•
The Electrochemical Society of Japan
•
Korea Electrochemical Society

Insights on the variability of Cu filament formation in the SiO₂ electrolyte of quantized-conductance conductive bridge random access memory devices

Florian Maudet^{1,*} , Adnan Hammud² , Markus Wollgarten³,
Veeresh Deshpande¹ and Catherine Dubourdieu^{1,4,*}

¹Institute Functional Oxides for Energy-Efficient Information Technology, Helmholtz-Zentrum Berlin für Materialien und Energie, Hahn-Meitner Platz 1, D-14109 Berlin, Germany

²Department of Inorganic Chemistry, Fritz-Haber Institute of the Max-Planck Society, Faradayweg 4-6, D-14195 Berlin, Germany

³Institut Solare Brennstoffe (CE-IF), Helmholtz-Zentrum Berlin für Materialien und Energie, Hahn-Meitner Platz 1, D-14109 Berlin, Germany

⁴Freie Universität Berlin, Physical Chemistry, Arnimallee 22, D-14195 Berlin, Germany

E-mail: florian.maudet@helmholtz-berlin.de and catherine.dubourdieu@helmholtz-berlin.de

Received 26 August 2022, revised 3 January 2023

Accepted for publication 17 February 2023

Published 29 March 2023



CrossMark

Abstract

Conductive bridge random access memory devices such as Cu/SiO₂/W are promising candidates for applications in neuromorphic computing due to their fast, low-voltage switching, multiple-conductance states, scalability, low off-current, and full compatibility with advanced Si CMOS technologies. The conductance states, which can be quantized, originate from the formation of a Cu filament in the SiO₂ electrolyte due to cation-migration-based electrochemical processes. A major challenge related to the filamentary nature is the strong variability of the voltage required to switch the device to its conducting state. Here, based on a statistical analysis of more than hundred fifty Cu/SiO₂/W devices, we point to the key role of the activation energy distribution for copper ion diffusion in the amorphous SiO₂. The cycle-to-cycle variability is modeled well when considering the theoretical energy landscape for Cu diffusion paths to grow the filament. Perspectives of this work point to developing strategies to narrow the distribution of activation energies in amorphous SiO₂.

Supplementary material for this article is available [online](#)

Keywords: CBRAM, quantum conductance, SiO₂, stochasticity, neuromorphic computing, analytical model, electrochemical metallization cell (ECM)

(Some figures may appear in colour only in the online journal)

Introduction

Recently extensive work has been conducted to study and enhance the performances of resistive switching memristive devices as they are promising candidates for the next generation of nonvolatile random access memories or for neuromorphic applications [1–3]. Of all the studied

* Authors to whom any correspondence should be addressed.

configurations, conductive bridge random access memory (CBRAM), also named electrochemical metallization cell (ECM), holds great potential as it offers the possibility of fast switching, multiple states, ultimate scaling for ultra large scale integration, and low power consumption [4–6]. The possibility in such systems to obtain multiple state resistance values is of great interest for neuromorphic applications. SiO₂-based CBRAM have been studied with a variety of active electrodes, mainly Ag and Cu [7–10] and more recently Co [11]. The different resistance states are governed by the formation or dissolution of a metallic filament (Cu, Ag) in the dielectric SiO₂ solid electrolyte [7, 8, 12]. When a positive bias is applied (on the active electrode), metallic ions migrate through the solid electrolyte, which leads to the electro-deposition of the metal (Cu, Ag) on the passive W electrode. Once the conductive filament bridges both electrodes, the device is in a low resistive state. Upon a negative bias, the metallic filament is dissolved by the migration of metallic ions (Cu, Ag) out of the filament [13]. The Cu/SiO₂/W system offers the advantage of being fully CMOS compatible [14–22]. This stack was shown to exhibit quantized quantum conductance states and a remarkably low operating power [21]. One of the major challenge for the integration of CBRAM in practical applications remains their stochasticity [4]. There is a lack of systematic statistical studies in literature for a clear understanding of these devices.

In this paper, we first present an analysis of the quantum conductance state distribution in Cu/SiO₂/W CBRAM devices and show that it varies quite significantly when increasing the programming current. To understand the origin of this variability, we then focus on the *I*–*V* curves and particularly on the SET voltage, which relates to the Cu filament formation. The cycle-to-cycle SET voltage variability is measured on more than hundred fifty devices and analyzed with a physical model.

Results

The stack in our devices consists of a 135 nm W bottom inert electrode deposited by sputtering on a p-type Si substrate with 300 nm thermal oxide, a 10 nm SiO₂ film deposited by plasma-enhanced chemical vapor deposition as the electrolyte and a top 70 nm Cu active electrode deposited by sputtering. The top electrode is capped with 90 nm Au (with a 2 nm Ti seed layer underneath) to avoid oxidation of the Cu electrode with time. On figure 1(a) a TEM cross section image of the device cross-point is presented. No evidence of copper diffusion in the 10 nm SiO₂ matrix is observed from EDX mapping (see figure S1 of the supplementary materials). From the EDX analysis (described in the supplementary materials) an atomic ratio of 33% ± 15% at. Si/67% ± 15% at. was determined. Since the uncertainty of the EDX analysis is quite large, we further investigated the physical properties of 10 nm SiO₂ films by spectroscopic ellipsometry measurements (described in the supplementary materials). The refractive index and extinction coefficient spectra (figure S2), compared to those of a 300 nm thermally-grown SiO₂ reference, show

that the PECVD-grown films consist of dense and near-stoichiometric SiO₂.

The active Cu/SiO₂/W device is a targeted cross-point of 30 μm × 30 μm (measured on average as 31 ± 0.5 × 30 ± 0.5 μm²), fabricated using conventional photolithography with unpatterned bottom electrode (figure 1(b)).

For the statistical analysis, a batch consisting of three samples was processed, each sample being composed of 4 dies and each die of 13 devices (figures 1(b)–(d)), hence providing a total of 156 devices. The samples were stored under N₂ atmosphere with desiccant. A pinched hysteresis *I*–*V* curve characteristic of the bipolar resistive switching in our CBRAMs is shown in figure 1(e) for a typical device. During a positive sweep, the devices transition (SET transition) from a high resistive state (HRS)—the OFF state—to a low resistive state (LRS)—the ON state. No forming step is required to form the first filament. Very low voltages, typically below 450 mV are required for the SET operation (compliance current of 100 μA). Upon negative voltage sweep, the devices are RESET (transition from LRS to HRS) at voltages typically around –100 mV. As previously reported [21], these devices exhibit half-integer quantized quantum conductance states that are clearly evidenced when performing a current sweep as shown in figure 1(f). Indeed, when the lateral dimension of the conducting channel is comparable to the Fermi wavelength (λ_F) and the transverse dimension is smaller than the mean free path (ballistic transport), the conductance of nanoscale devices can exhibit discrete quantized states. The Landauer theory for ballistic electron transport predicts—in the case of a single conduction channel—that $G_0 = \frac{2e^2}{h}$ is the quantum of conductance, where *e* is the charge of electron, *h* is the Planck's constant and the factor 2 accounts for spin degeneracy [23]. For multiple channels the conductance will be *N* *G*₀ where *N* is an integer. The size of the filament defines the integer *N*. In CBRAM devices the size of the filament can be controlled by the supplied current. The voltage is the driving force of the ion diffusion; the electronic current leads to the reduction of Cu²⁺ ions to Cu and contributes to the growth of the conducting filament. The compliance on the current limits the current flow, which stops the lateral growth of the filament. Different lateral dimensions will lead to different quantized conductance states. The filament dimension can be calculated as described in [21]. The half-integer multiples of *G*₀ could be explained mathematically by the presence of energy sub-bands in the Fermi level split between contact reservoirs [21]. As a matter of fact, not only half-integer but also quarter-integer quantum conductance states are observed, whose origin will be discussed elsewhere.

For a compliance current of 100 μA, the median retention time of the devices is typically of 1 to 10 s. Such volatile devices are of interest for enabling brain inspired algorithms.

Variability of the quantum conductance states

The occurrence of several well-defined conductance states is of high interest for neuromorphic computation. However, for practical use, the states should be distinguishable and

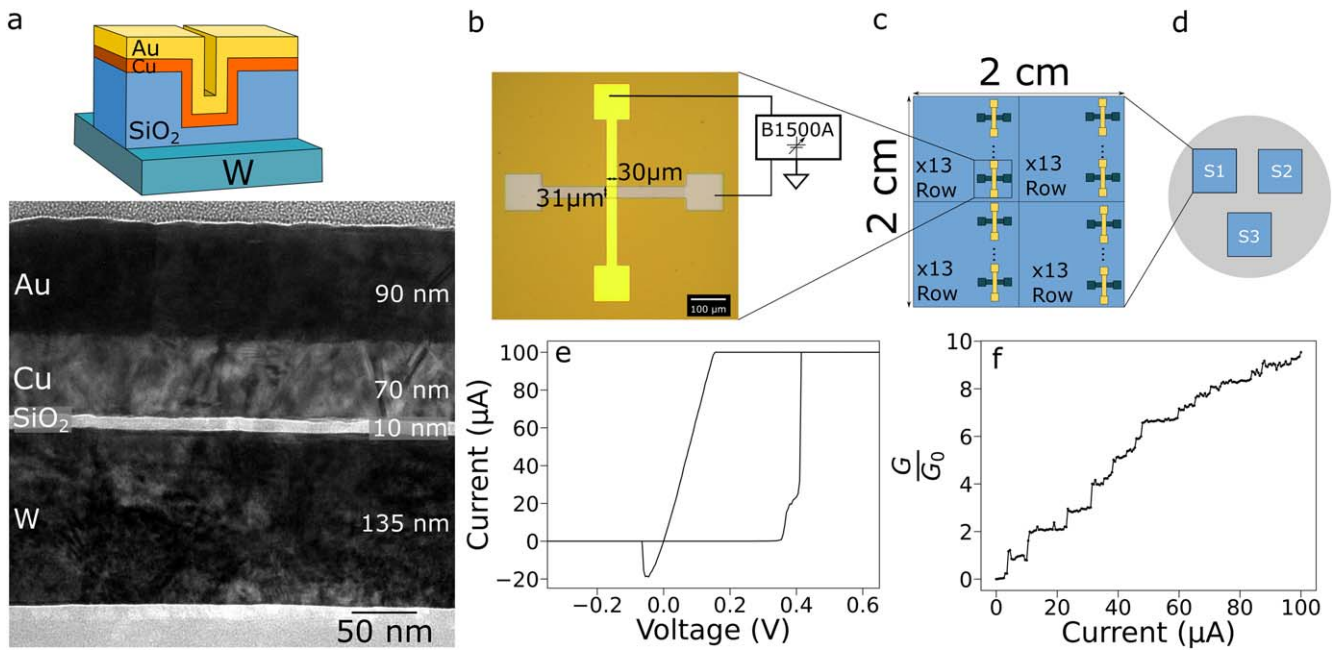


Figure 1. Devices under study. (a) Schematic of the device stack and TEM cross section image of the cross point. (b) Optical top-view microscopy image of the cross point with measurement scheme. (c) Typical $2 \times 2 \text{ cm}^2$ Si samples on which the devices are prepared with 4 dies and 13 devices on each die. (d) Positioning of the samples in each batch preparation. (e) Typical pinched hysteresis I - V curve measured with a compliance current of $100 \mu\text{A}$ and plotted in linear scale. (f) Example of quantum conductance curve versus current observed in the devices.

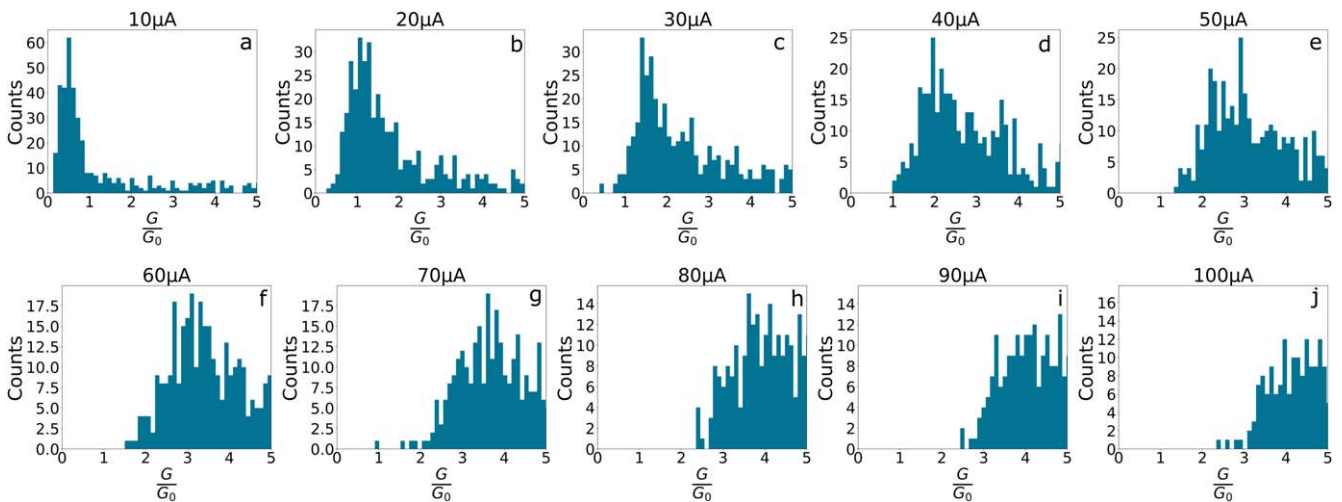


Figure 2. Quantum conductance state distribution for compliance current of: (a) $10 \mu\text{A}$, (b) $20 \mu\text{A}$, (c) $30 \mu\text{A}$, (d) $40 \mu\text{A}$, (e) $50 \mu\text{A}$, (f) $60 \mu\text{A}$, (g) $70 \mu\text{A}$, (h) $80 \mu\text{A}$, (i) $90 \mu\text{A}$ and (j) $100 \mu\text{A}$. The distribution is cumulative of all devices and all cycles performed.

controllable. We show in figure 2 the distribution of the quantum conductance values measured for different programming currents ranging from 10 to $100 \mu\text{A}$ (with a compliance voltage of 1 V) on a total of 26 devices (2 dies) with 30 cycles performed on each device.

For a low programming current of $10 \mu\text{A}$ (figure 2(a)) the quantum conductance state distribution is relatively narrow and centered at $0.5 G_0$, suggesting that this state can repeatedly be programmed using a $10 \mu\text{A}$ current. For an increasing programming current, the distribution shifts to higher conductance states, and gets broader. The quantum conductance G is related to the diameter of the filament

formed [21]. G values are clearly increased for larger currents but also appear more random. At least three differentiable memory states, (0.5 - $1 G_0$, 1.5 - $3 G_0$ and 3 - $5 G_0$) are available in the programming current range of 10 - $100 \mu\text{A}$. The broadening of the quantum conductance state distribution clearly limits the potential of such devices. To improve this aspect, it is therefore key to understand the origin of the variability in such devices.

Variability of SET voltages

We have focused our analysis on the SET voltages of the devices, which correspond to the transition from OFF to ON

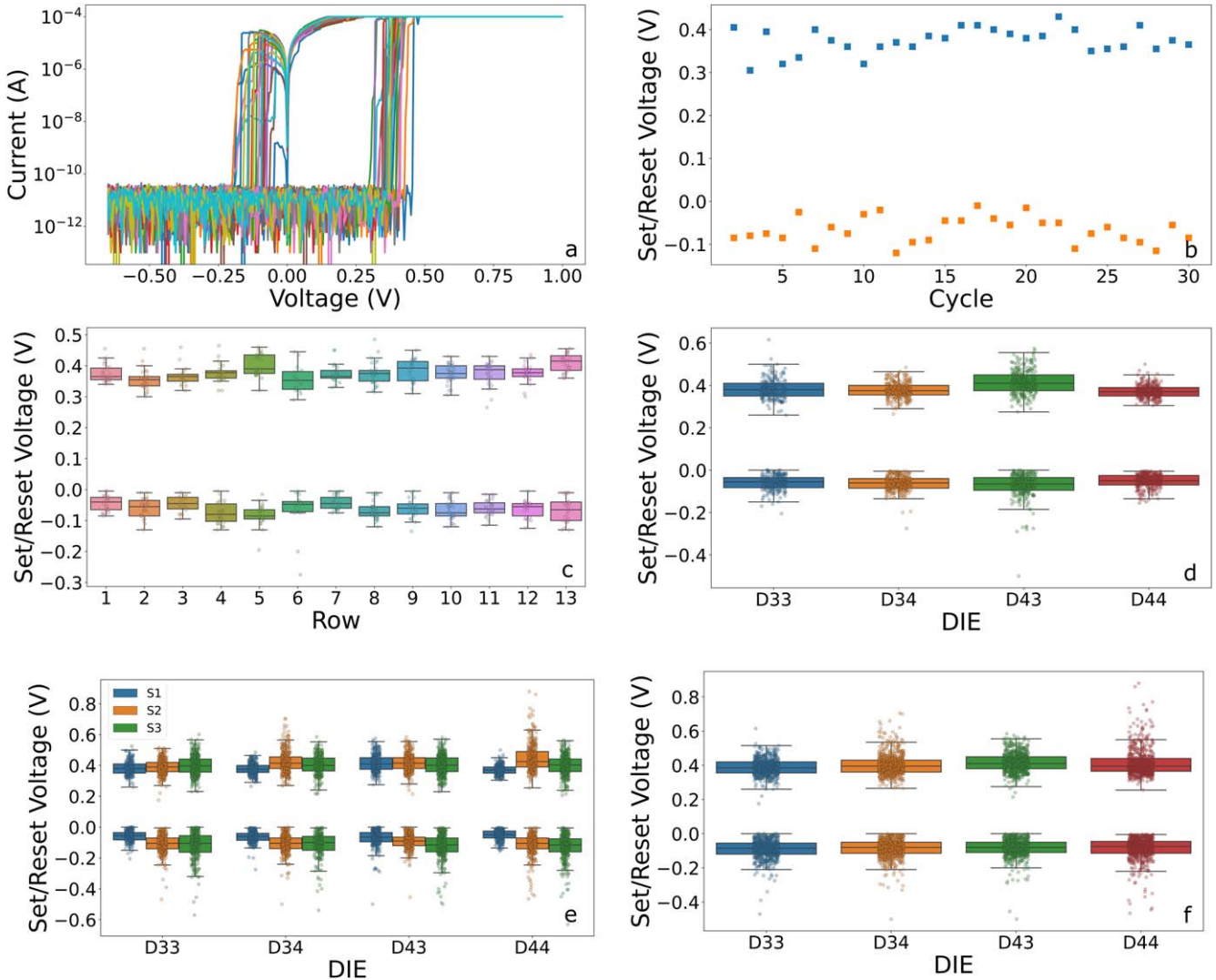


Figure 3. Statistical analysis of I - V sweep measurements. (a) Thirty I - V cycles of a representative device. (b) SET and RESET voltages of the device shown in (a). (c) SET and RESET voltages obtained for 13 devices from one die. (d) SET and RESET voltages for 4 dies of a same sample—(e) SET and RESET voltages for 4 dies of three samples of the same batch (total of 156 devices)—(f) SET and RESET voltages for all 156 devices. For (c)–(f), the rectangles of the boxplots represent the first and third quartiles and the bars the 5th and 95th centiles.

states. The device-to-device, die-to-die or sample-to-sample variations have been studied on a large number of devices (156 devices) in order to distinguish the intrinsic variability—clearly observed upon cycle-to-cycle measurements—from potential extrinsic variability. Cycle-to-cycle variation is associated with the intrinsic physical stochasticity of the device. Device-to-device/die-to-die and especially sample-to-sample variations originate not only from the intrinsic stochasticity but also from fabrication process related effects like thickness inhomogeneity, deposition processes variations, processing residues, etc. For each of these devices, thirty full I - V cycles were measured with a sweep rate of $2.5 \cdot 10^{-2} \text{ V.s}^{-1}$ and for the statistical analysis, only devices showing at least fifteen full I - V cycles were considered.

In figure 3(a) thirty consecutive I - V sweep cycles are shown for a representative device. The device exhibits a high $R_{\text{ON}}/R_{\text{OFF}}$ ratio of $\sim 10^6$ obtained repeatedly with a relatively narrow SET and RESET voltage distribution. This repeatability implies that the RESET process is complete, i.e. the

conductive paths are completely removed in the RESET sweep or are below the detection limit. An incomplete RESET would indeed lead to a lowering of the SET voltage in the succeeding SET sweep. In figure 3(b), the corresponding SET and RESET voltages are presented. Low median values of the SET voltage ($0.385 \pm 0.062 \text{ V}$) and RESET voltage ($-0.081 \pm 0.032 \text{ V}$) are obtained. For all measured devices, the first cycle is not different from the following ones and stays within the overall voltage distribution. This observation supports the completeness of the RESET process. Now, we consider the SET and RESET distribution of thirty cycles on each device for different devices of a single die, of different dies, of different samples as shown in figures 3(c)–(f), respectively. In figure 3(c), the boxplot underlines the relatively high homogeneity of the devices on a single die, with the exception of one or two of them. The four dies (figure 3(d)) of one sample exhibit consistently reproducible values of voltage median and distribution in SET and RESET voltages, apart from one die (D43) that has a slightly broader

Table 1. Median value, standard deviation and difference between the third and first quartile of the SET voltage values for different sampling size. For each device, 30 cycles were measured (a batch of 3 samples represents 4680 measurements).

	30 cycles 1 device	1 die 13 devices	4 dies = 1 sample 52 devices	Batch = 3 samples 156 devices
Median V_{set}	0.385 V	0.410 V	0.410 V	0.395 V
$\sigma_{V_{\text{set}}}$	0.062 V	0.065 V	0.069 V	0.065 V
Q_3-Q_1	0.071 V	0.075 V	0.075 V	0.070 V

distribution of the SET voltage. This observation highlights the importance of the analysis of a large number of devices as the sole analysis of the die D43 could have led to a skewed picture. A relatively good sample-to-sample repeatability is also observed for the three samples processed within the same batch (figures 3(e), (f)).

To summarize the results on the switching variability - from OFF to ON states - of the 156 devices under study, we give in table 1 the median value and the standard deviation of their SET voltage values ($\sigma_{V_{\text{set}}}$) and the difference between the third and first quartile (Q_3-Q_1) for different sampling size, representative of the cycle-to-cycle, device-to-device, die-to-die and sample-to-sample variabilities.

The median SET value of the different devices is comprised between 385 and 410 mV with a low dependence on the sampling size indicating a low device-to-device variability. A relatively low cycle-to-cycle variation of the SET voltages is observed for a single device (0.062 V). The standard deviation observed for one die (0.065 V) is very close to the dispersion of a single device. For the four dies of a sample as well as for the three samples in the batch, similar values of SET voltage dispersion $\sigma_{V_{\text{set}}}$ are observed as compared to the device-to-device one on a single die, with 0.069 V and 0.065 V respectively. The similar trend observed for the difference between the first and third quartile is indicative of a normal distribution of the set values. These observations confirm that the cycle-to-cycle variability is the major cause of the dispersion of the SET values and that the fabrication can be controlled to achieve homogenous samples leading to a negligible device-to-device variation.

A comparison to median set voltages and standard deviations from other works on similar stacks is presented in table 2.

Note that these CBRAM devices usually rely on an initial forming process needed before cycling. A direct comparison with our devices is therefore not straightforward. However, it is interesting to note that similar values of the set voltage and standard deviation are observed from comparable stacks independent of the deposition method [15, 24]. However, for SiO₂ films with a larger thickness, a larger median set voltage and standard deviation are measured [25, 26]. This behavior highlights the importance of the copper diffusion mechanism in determining the set voltage value.

Discussion on the SET voltage distribution

It is now well admitted that switching of these Cu/SiO₂/W devices is governed by the formation of a Cu metallic filament as a result of oxido-reduction processes occurring at the active and passive electrodes [27, 28]. Once the copper ions are formed under electrochemical oxidation, they diffuse through the electrolyte SiO₂ under the applied electric field [29]. For this to happen copper ions must have enough energy to overcome the energy barriers of the different sites encountered in the amorphous SiO₂ electrolyte where the local environment varies (figure 4(a)). The different binding environments will lead to more or less ‘easy’ and ‘hard’ diffusion paths (with respectively lower and larger activation energies), which inherently leads to stochasticity. Guzman *et al* have modelled the migration of copper atoms and clusters in amorphous SiO₂ using density functional theory and report a broad distribution of activation energies for Cu migration, ranging from 0.2 to 1.2 eV as shown in figure 4(b) [30]. Hence, for different nucleation position of the filament, copper ion migration will happen at different rates.

A model can be developed to analyze the influence of this distribution of activation energies on the SET voltage distribution. Different approaches have been proposed to model the behavior of CBRAM devices: finite elements, kinetic Monte Carlo, analytical, and compact models [10, 31, 32]. Among them, analytical models constitute a relatively simple approach to predict the impact of physical properties of the material on the device performances. When taking into account all physical mechanisms at play for the device behavior, analytical models have to be solved numerically as it leads to equations with an implicit form [31]. However, under reasonable assumptions these equations can be solved analytically. Here, to find out the impact of the distribution of activation energies on the distribution of SET voltages, an analytical model assuming that migration of Cu is the limiting factor for the filament formation was used [32]. Five hypotheses are made, defining the range of validity of this model. First, we consider that the devices do not have a cycle history i.e. the RESET is complete, which is supported by the repeatability of the OFF state (RESET voltage) and by the absence of forming voltage, suggesting the formation of a new filament for each cycle. Second, the influence of temperature on the filament is neglected as we consider only SET voltages happening under low current (<nA) and thus low joule heating effect. Third, copper migration is supposed to be the limiting mechanism of the switching process. Fourth, the filament is assumed to grow vertically before lateral expansion occurs [33]. Finally, the nucleation of the filament is assumed to happen at random locations as it will be sensitive to noise in the electric field. Therefore, this model can be applied to devices with a complete reset process with a high off-resistance state where copper diffusion is the limiting mechanism.

Following these assumptions the growth rate of a cylindrical filament of height h can be modeled by the

Table 2. Median set and standard deviation comparison from this work and literature.

Median V_{set} (V)	$\sigma_{V_{\text{set}}}$	Number of cycles/devi- ces for $\sigma_{V_{\text{set}}}$	Stack	SiO ₂ deposition method	Thickness (nm)	Temperature measurements	Mechanism	Reference
0.310	0.025	100/1	Cu/SiO ₂ /W	Magnetron sputtering	10	No	Red/Ox metallic filament formation	[24]
0.357	0.062	Not specified	Cu/SiO ₂ /W	Electron beam evaporation	13	No	Red/Ox metallic filament formation	[15]
0.853	0.156	150/1	Cu/SiO ₂ /Ni	HSQ spin coat e-beam exposure	100-55	Yes	Conduction fit a metallic behavior	[25]
0.762	0.189	100/1	Cu/SiO ₂ /Pt	Magnetron sputtering	20	No	Metallic filament	[26]
0.395	0.065	30/156	Cu/SiO ₂ /W	PECVD	10	No	Red/Ox metallic filament formation	This work

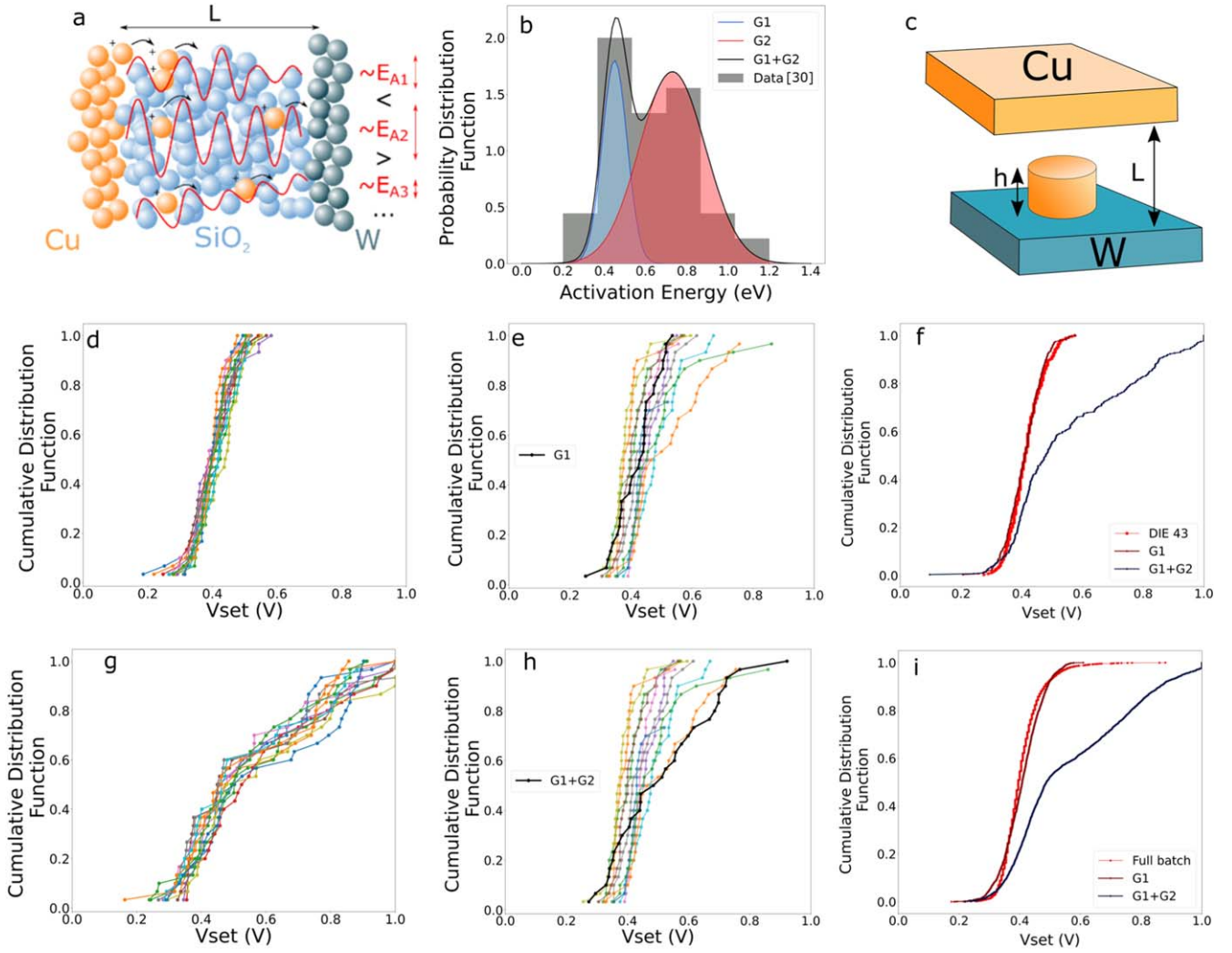


Figure 4. Modelling of the variability of the SET voltages—(a) Schematic representation of the Cu ion drift process. (b) Probability distribution function of the activation energies for copper diffusion in amorphous SiO₂ as calculated by DFT in [30] together with our fit with two Gaussians G1 and G2. G1 corresponds to ‘easy’ diffusion paths in SiO₂. For the simulations of the cumulative V_{SET} distributions (equation (3)), we used either G1 only or G1 + G2 functions. (c) Schematic depicting the analytical model used for filament growth. (d), (g) Simulated cumulated V_{SET} distribution functions for 13 devices (with 30 cycles each) using the Gaussian function G1 only (d) or G1 + G2 (g). (e), (h) Experimental cumulative V_{SET} distribution functions from the measured 13 devices (30 cycles per device) of one die together with a simulated distribution example shown in black (for 30 cycles) using G1 only (e) and G1 + G2 (h). (f), (i) Experimental (red) cumulative V_{SET} distribution function from all devices measured on a single die (f) and from all devices of the three-sample batch (i) together with two simulated distribution examples using G1 only (brown curve) and G1 + G2 (black curve).

following Arrhenius law [32, 34]:

$$\frac{dh(t)}{dt} = v_h e^{-\frac{(E_a - q\alpha V)}{kT}} = v_h e^{-\frac{(E_a - q\alpha\beta t)}{kT}}, \quad (1)$$

where the constant v_h is an exponential prefactor, E_a is the activation energy for Cu ion migration (eV), V is the voltage drop across the gap between the filament and the inert electrode, q is the electron charge, α is the barrier lowering factor, k is the Boltzmann constant and T is the temperature of the ions.

As the applied voltage is swept, the factor βt is introduced to take into account the voltage dependence over time where β is the voltage sweep rate ($V \cdot s^{-1}$), t is the time (s).

The height h is then directly expressed by:

$$h(t) = \frac{v_h kT}{q\alpha\beta} e^{-\frac{(E_a - q\alpha\beta t)}{kT}}. \quad (2)$$

We define the SET point of the device for $h = L$ where L is the SiO₂ dielectric thickness, i.e. when the filament has bridged top and bottom electrodes. Consequently, the SET voltage is expressed by:

$$V_{set} = \frac{E_a + \ln\left(\frac{Lq\alpha\beta}{v_h kT}\right)kT}{q\alpha}. \quad (3)$$

Table 3. Values of the parameters used for the analytical model.

Symbol	Value
E_a	G1($A = 1.8$, $\mu = 0.43$ eV, $\sigma = 0.06$ eV) G2($A = 1.7$, $\mu = 0.73$ eV, $\sigma = 0.16$ eV)
v_h	5.10^{-7} m.s ⁻¹
α	0.95
β	$2.5.10^{-2}$ V.s ⁻¹
L	10 nm

This expression allows us to compute the SET voltage distribution in our devices. The parameter used for the calculation of V_{SET} are summarized in table 3. The length L corresponds to the thickness of the film and β is the sweep rate of our measurement. A schematic of the model is presented in figure 4(c). As for the activation energy E_a , we have considered the distribution of activation energies calculated by Guzman *et al* for copper ion diffusion in amorphous SiO₂ [30]. These theoretical calculations highlight that different local binding configurations in the amorphous SiO₂—leading to copper diffusion paths easier than others as they provide more or less space for cation species to move—result in different activation energies. We fitted the distribution reported in [30] with two Gaussians (G1 and G2) as shown on figure 4(b). The G1 distribution corresponds to intrinsic ‘easy’ diffusion paths in amorphous SiO₂. Only v_h and α are free parameters, which were adjusted so that the median SET value of the model corresponds to the one of the full set of devices. We found $v_h = 5.10^{-7}$ m.s⁻¹ which is similar to the value of 8.10^{-7} m.s⁻¹ that is calculated from 20 assuming a diffusion coefficient of Cu in SiO₂ of $D_0 = 1.10^{-10}$ cm².s⁻¹. To the best of our knowledge no value is available for α for comparison but the obtained value of 0.95 is physical ($0 < \alpha < 1$) and reasonable with the thickness considered.

Using equation (3) the variance of the SET voltage can be determined analytically. In the ideal case of a perfectly smooth surface ($\sigma_L = 0$) and homogenous sample ($\sigma_{v_h} = 0$) it is expressed as:

$$\sigma_{V_{set}} = \frac{\sigma_{E_a}}{q\alpha}. \quad (4)$$

This constitutes the minimum intrinsic variability of the SET voltage of a device in this model, that depends on α and on the distribution of activation energies in SiO₂.

In the calculation of the SET voltage cumulative distributions shown in figures 4(d) and (g), we have considered two cases: the distribution of the activation energies E_a is represented by the sum of the two Gaussian functions G1 + G2 or by only the G1 Gaussian (the ‘easy’ diffusion paths distribution). The G1 + G2 Gaussian of activation energies lead of course to a much larger SET voltage variability (80% of the SET values are comprised between 0.34 and 0.87 V) as compared to the one obtained with G1 alone (0.34 and 0.48 V). On figures 4(e) and (h) we represent the experimental cumulative distributions of the SET voltages for thirteen devices (one die) and a calculated curve using G1 and G1 +

G2 respectively. Most of the measured cumulative SET distributions are very well modelled using only the G1 function. This result indicates that at least one diffusion path with an energy landscape that does not exceed 0.43 eV is always available for the Cu ions diffusing in the SiO₂ electrolyte so that this path is favored. We do not have information on the relative distributions of the different binding configurations in SiO₂ considered for the calculations of activation energies. The intrinsic ‘easy’ diffusion paths as calculated in [30] might be available in a large extent in our amorphous SiO₂ films. However, we cannot preclude the possibility of additional low energy paths of extrinsic origin (impurities, etc). From the spectroscopic ellipsometry measurements, which point to dense SiO₂ films, we can exclude porosity as an origin of easy diffusion paths in our devices.

A very good match is also obtained for the concatenated results of the cumulative distribution functions of a die and of the 156 devices (figures 4(i), (f)). The simulation based on the full Gaussian distribution of the activation energy (G1 + G2) only represents few cases as shown in figure 4(h). Of the total of 156 devices, 9 devices exhibited a SET value larger than 0.60 V.

The theoretical standard deviation for the G1 distribution is calculated to be $\sigma_{V_{set G1}} = 0.063$ V close to the standard deviation observed experimentally for different sampling size (single device, single die, single sample, and full batch) as shown in table 1. The theoretical standard deviation of G1 + G2 is calculated to be $\sigma_{V_{set G1+G2}} = 0.175$ V representing a larger distribution of the SET voltage.

The good agreement between experiments and the calculated V_{set} distributions indicates that the variability originates—at least to a large extent—from the distribution of activation energies centered about 0.43 eV for the diffusion of copper ions in the SiO₂ amorphous matrix.

Conclusion

We characterized and analyzed the stochasticity of the SET voltages of 156 Cu/SiO₂/W CBRAM devices. For the electrolyte produced here by PECVD at low temperature (120 °C), the median SET value of the 156 devices is of 0.395 V with a standard deviation of 0.065 V, whereas the cycle-to-cycle standard deviation is of 0.062 V. The cycle-to-cycle variability was examined using an analytical model including a distribution of activation energies for Cu ion diffusion in amorphous SiO₂, from a reported DFT calculation. The cycle-to-cycle stochastic SET behavior appears intrinsically related to the energy landscape of the diffusion paths available in the amorphous SiO₂ and is reproduced very well by considering diffusion paths with a relatively low variability in energy (0.060V) and an average barrier height of 0.43 eV. Only few devices (9 out of 156) exhibit a behavior indicative of a much larger activation energy distribution. The minimization of the available diffusion paths in SiO₂ is key to narrow the variability of the SET and RESET voltages. With this statistical study, we also show that the device-to-device variability is similar to the cycle-to-cycle one, which is the result of a

controlled process of the device fabrication. Future perspective of this work includes the integration of such devices in the back-end-of-line of CMOS chips and on flexible substrates for the development of stochastic neuromorphic systems [35].

Methods

Device fabrication

A 135 nm W layer was deposited by sputtering at room temperature on 300 nm thermally grown SiO₂ on Si substrates. A thick insulator layer of 200 nm SiO₂ was then deposited by PECVD at 120 °C and patterned by lift-off using photolithography. A blanket deposition of 10 nm SiO₂ was performed also by PECVD at 120 °C for the active electrolyte layer. Then, 70 nm Cu followed by 2 nm Ti/90 nm Au capping layers were deposited by thermal evaporation and patterned by lift-off to create 30 × 30 μm² cross point. Finally, the bottom pads were opened to guarantee a good ohmic contact to the bottom electrode by reactive ion etching of the 10 nm SiO₂ layer using CHF₃/Ar.

(S)TEM and EDX analyses

A TEM lamella was prepared from the center of a 30 μm × 30 μm device cross point by gallium focused ion beam (FIB). Layers of Pt were deposited by e-beam and ion beam deposition to protect the device layers during FIB lamella preparation. The lamella was cut parallel to Si ⟨110⟩ (parallel to sample edge). Microscopy experiments were done using a Zeiss LIBRA 200 FE transmission electron microscope (TEM/STEM), operated at 200 kV. The TEM/STEM is equipped with an in-column energy filter which was used to obtain zero loss filtered images at various magnifications. EDX analyses were done using a Thermo Noran system, six detector and accompanying electronics in STEM mode. EDX stoichiometric quantification was made following the Cliff Lorimer method [36]. The Si Kα (1.74 keV) and O Kα (0.52 keV) peaks were used to fit the atomic ratio on the SiO₂ layer using a k_{Fe} factors of 0.76 ± 0.08 and 1.9 ± 0.2 respectively [36–38].

Spectroscopic ellipsometry study

The thickness and optical index of the SiO₂ films were determined by spectroscopic ellipsometry (Woollam M2000) at three different incidence angles (60°, 65° and 70°), in a wavelength range of 192–1686 nm. To model the ellipsometric data of the SiO₂ layer, a two-layer stack model was used. First a measurement was done on the tungsten layer that can directly be inverted to calculate its optical properties as it can be considered as a half infinite substrate. A layer modeled by a Cauchy-Urbach dispersion law was then added on top of the W substrate to fit the SiO₂/W stack.

Electrical measurements

Electrical measurements were performed on a MPI TS2000-SE probe station with Keysight B1500A semiconductor parameter analyzer on 30 × 30 μm² cross point devices. Voltage-current measurements (30 cycles for each device) were performed for the determination of the quantized conductance on the thirteen devices for two dies on one sample. The current was swept from 10 μA to 100 μA with a compliance voltage of 1 V. For the SET value study, current-voltage measurements were performed (30 cycles for each device) with current compliance of 100 μA and a sweep rate of 0.025 V.s⁻¹ on each of the thirteen devices of the four dies for three samples.

Acknowledgments

All authors acknowledge Stefan Bock, Luca Sulmoni and Ronny Schmidt for technical support at the clean room of the Physics Department of the Technische Universität Berlin.

Data availability statement

The data that support the findings of this study are openly available at the following URL/DOI: <https://doi.org/10.5281/zenodo.7646646>.

Additional information

Correspondence and requests for materials should be addressed to C.D. or F.M.

ORCID iDs

Florian Maudet  <https://orcid.org/0000-0001-8498-7727>
Adnan Hammud  <https://orcid.org/0000-0001-5580-7985>

References

- [1] 2003 *Rainer Waser* Waser R (ed) (Weinheim: Wiley-VCH)
- [2] Yang J J, Inoue I H, Mikolajick T and Hwang C S 2012 *MRS Bull.* **37** 131–7
- [3] Ielmini D 2016 *Semicond. Sci. Technol.* **31** 063002
- [4] Valov I, Waser R, Jameson J R and Kozicki M N 2011 *Nanotechnology* **22** 289502
- [5] Onofrio N, Guzman D and Strachan A 2015 *Nat. Mater.* **14** 440–6
- [6] Kozicki M N and Barnaby H J 2016 *Semicond. Sci. Technol.* **31** 113001
- [7] Schindler C, Weides M, Kozicki M N and Waser R 2008 *Appl. Phys. Lett.* **92** 1–4
- [8] Tappertzshofen S, Mündelein H, Valov I and Waser R 2012 *Nanoscale* **4** 3040
- [9] Tappertzshofen S, Waser R and Valov I 2013 *13th Non-Volatile Mem. Technol. Symp. NVMTS* 1–5

- [10] Wang W, Laudato M, Ambrosi E, Bricalli A, Covi E, Lin Y H and Ielmini D 2019 *IEEE Trans. Electron Devices* **66** 3795–801
- [11] Belmonte A et al 2019 *2019 IEEE Int. Electron Devices Meeting (IEDM) vol 2019-Decem (IEEE)* pp 8.1–8.4
- [12] Mehonic A et al 2018 *Adv. Mater.* **30** 1–21
- [13] Tappertzhofen S, Menzel S, Valov I and Waser R 2011 *Appl. Phys. Lett.* **99** 1–4
- [14] Bernard Y, Renard V T, Gonon P and Jousseume V 2011 *Microelectron. Eng.* **88** 814–6
- [15] Chen W, Barnaby H J, Kozicki M N, Edwards A H, Gonzalez-Velo Y, Fang R, Holbert K E, Yu S and Yu W 2015 *IEEE Trans. Nucl. Sci.* **62** 2404–11
- [16] Wang M et al 2010 *2010 Symp. on VLSI Technology (IEEE)* pp 89–90
- [17] Catenacci M J, Flowers P F, Cao C, Andrews J B, Franklin A D and Wiley B J 2017 *J. Electron. Mater.* **46** 4596–603
- [18] Thermadam S P, Bhagat S K, Alford T L, Sakaguchi Y, Kozicki M N and Mitkova M 2010 *Thin Solid Films* **518** 3293–8
- [19] Chen W, Tappertzhofen S, Barnaby H J and Kozicki M N 2017 *J. Electroceramics* **39** 109–31
- [20] Tappertzhofen S, Mündelein H, Valov I and Waser R 2012 *Nanoscale* **4** 3040
- [21] Nandakumar S R, Minvielle M, Nagar S, Dubourdieu C and Rajendran B 2016 *Nano Lett.* **16** 1602–8
- [22] Mehonic A et al 2018 *Adv. Mater.* **30** 1801187
- [23] Landauer R 1988 *IBM J. Res. Dev.* **32** 306–16
- [24] Cao H and Ren H 2022 *Appl. Phys. Lett.* **120** 133502
- [25] Rice Z P, Briggs B D, Bishop S M and Cady N C 2012 *J. Mater. Res.* **27** 3110–6
- [26] Li Y, Yin L, Wu Z, Li X, Song X, Gao X and Fu L 2019 *IEEE Electron Device Lett.* **40** 1599–601
- [27] Yang Y, Gao P, Li L, Pan X, Tappertzhofen S, Choi S, Waser R, Valov I and Lu W D 2014 *Nat. Commun.* **5** 4232
- [28] Yuan F, Zhang Z, Liu C, Zhou F, Yau H M, Lu W, Qiu X, Wong H S P, Dai J and Chai Y 2017 *ACS Nano* **11** 4097–104
- [29] Wang W, Covi E, Lin Y-H, Ambrosi E and Ielmini D 2019 *2019 IEEE Int. Electron Devices Meeting (IEDM) vol 2019-Decem (IEEE)* pp 3.1–3.4
- [30] Guzman D M, Onofrio N and Strachan A 2015 *J. Appl. Phys.* **117**
- [31] Menzel S 2017 *J. Comput. Electron.* **16** 1017–37
- [32] Wang W, Laudato M, Ambrosi E, Bricalli A, Covi E, Lin Y H and Ielmini D 2019 *IEEE Trans. Electron Devices* **66** 3802–8
- [33] Nandakumar S R and Rajendran B 2016 *2016 Int. Conf. on Simulation of Semiconductor Processes and Devices (SISPAD) (IEEE)* pp 169–72
- [34] Ren Y, Tao Y, Li X, Wang Z, Xu H, Ielmini D, Lin Y, Zhao X and Liu Y 2020 *Semicond. Sci. Technol.* **35** 02LT01
- [35] Covi E, Lancaster S, Slesazek S, Deshpande V, Mikolajick T and Dubourdieu C 2022 *2022 IEEE Int. Conf. on Flexible and Printable Sensors and Systems (FLEPS) (IEEE)* pp 1–4
- [36] Goldstein J I, Williams D B and Cliff G 1986 *Principles of Analytical Electron Microscopy* vol 7 (Boston, MA: Springer US) pp 155–217
- [37] Malac M and Egerton R F 1999 *Microsc. Microanal.* **5** 29–38
- [38] Cliff G, Maher D M and Joy D C 1984 *J. Microsc.* **136** 219–25